PHYSICAL REVIEW B **93**, 245149 (2016)

Self-organized charge puddles in a three-dimensional topological material

N. Borgwardt,[1] J. Lux,[2] I. Vergara,[1] Zhiwei Wang,[1,3] A. A. Taskin,[1,3] Kouji Segawa,[3] P. H. M. van Loosdrecht,[1]
Yoichi Ando,[1,3] A. Rosch,[2] and M. Grüninger[1,*]

[1] *II. Physikalisches Institut, Universität zu Köln, Zülpicher Strasse 77, D-50937 Köln, Germany*
[2] *Institut für Theoretische Physik, Universität zu Köln, Zülpicher Strasse 77, D-50937 Köln, Germany*
[3] *Institute of Scientific and Industrial Research, Osaka University, Ibaraki, Osaka 567-0047, Japan*

(Received 13 August 2015; revised manuscript received 31 December 2015; published 24 June 2016)

In three-dimensional (3D) topological materials, tuning of the bulk chemical potential is of crucial importance for observing their topological properties; for example, Weyl semimetals require chemical-potential tuning to the bulk Weyl nodes, while 3D topological insulators require tuning into the bulk band gap. Such tuning is often realized by compensation, i.e., by balancing the density of acceptors and donors. Here we show that in such a compensated 3D topological material, the possibility of local chemical-potential tuning is limited by the formation of self-organized charge puddles. The puddles arise from large fluctuations of the Coulomb potential of donors and acceptors. Their emergence is akin to the case of graphene, where charge puddles are already established as a key paradigm. However, there is an important difference: Puddles in graphene are simply dictated by the static distribution of defects in the substrate, whereas we find that puddles in 3D systems self-organize in a nontrivial way and show a strong temperature dependence. Such a self-organization is revealed by measurements of the optical conductivity of the bulk-insulating 3D topological insulator $\mathrm{BiSbTeSe_2}$, which pinpoints the presence of puddles at low temperatures as well as their surprising "evaporation" on a temperature scale of 30–40 K. The experimental observation is described semiquantitatively by Monte Carlo simulations. These show that the temperature scale is set by the Coulomb interaction between neighboring dopants and that puddles are destroyed by thermally activated carriers in a highly nonlinear screening process. This result indicates that understanding charge puddles is crucial for the control of the chemical potential in compensated 3D topological materials.

DOI: 10.1103/PhysRevB.93.245149

I. INTRODUCTION

After the discovery of three-dimensional (3D) topological insulators [1–4], new types of topological states of matter are intensely sought after [5–8]. As a result, 3D topological crystalline insulators [9–13], 3D Dirac semimetals [14–20], and 3D Weyl semimetals [21–27] have been discovered. In all of these materials, control of the bulk chemical potential is of fundamental importance to study their topological properties. In topological insulators and topological crystalline insulators, the chemical potential should be tuned into the bulk band gap so that only the surface carriers contribute to transport; similarly, the peculiar properties of 3D Dirac and Weyl semimetals such as the chiral anomaly [8] or Fermi-arc transport [28] only manifest themselves if the chemical potential is close to the Dirac/Weyl node. However, for compound materials it is very difficult to obtain perfectly stoichiometric, defect-free samples. For instance, single crystals of the prototypical topological insulators $\mathrm{Bi_2Te_3}$ and $\mathrm{Bi_2Se_3}$ typically show defect-induced charge carriers with densities above a few $10^{18}\,\mathrm{cm}^{-3}$ [29–35]. To realize bulk-insulating samples, compensation between donor-type and acceptor-type defects is often employed [4]. A drawback of this strategy is that it necessarily creates Coulomb disorder, i.e., randomly distributed ionized acceptors and donors [36]. In 3D topological materials, the consequences of compensation have not received much attention. For example, the residual bulk transport in compensated topological insulators such as $\mathrm{Bi_2Te_2Se}$ [31] or $\mathrm{Bi_{2-x}Sb_xTe_{3-y}Se_y}$ [37,38] is usually considered to be due to "impurity bands." The existence of impurity bands may explain, e.g., the observation of activated behavior with a *small* activation energy, i.e., substantially smaller than the intrinsic value given by half the gap size, $\Delta/2$ [38]. However, based on optical measurements of compensated $\mathrm{BiSbTeSe_2}$ and Monte Carlo simulations, we show that such a simplistic notion is not applicable in the case of compensated 3D topological materials.

In this context, an alternative explanation of the small activation energy in compensated 3D topological insulators has recently been suggested by Skinner, Chen, and Shklovskii [39–41] building on previous work [36]. They considered a perfectly compensated semiconductor ($N_D = N_A \equiv N_{\mathrm{def}}$, where N_D and N_A are the densities of donors and acceptors, respectively) with shallow donor and acceptor levels. In such a system, donors give electrons to acceptors, resulting in positively charged empty donors and negatively charged occupied acceptors. In this situation, however, the long-range Coulomb interactions necessarily enforce a reorganization of the charge distribution by the formation of large puddles, i.e., regions in the bulk which locally contain either p- or n-type carriers. The reason for puddle formation is that in a volume of size R^3, random fluctuations of the donor and acceptor densities N_D and N_A locally lead to an uncompensated charge of order $e\sqrt{N_{\mathrm{def}} R^3}$ and therefore to a Coulomb potential of order $e^2\sqrt{N_{\mathrm{def}} R^3}/(4\pi\varepsilon_0\varepsilon R)$, where ε denotes the dielectric constant and e the elementary charge. These potential fluctuations grow in proportion to $\sqrt{R}$ and become as large as $\Delta/2$ at a length scale $R_g = (\Delta/E_c)^2\, d_{\mathrm{def}}/8\pi$ [39], where $d_{\mathrm{def}} = N_{\mathrm{def}}^{-1/3}$ denotes the average defect distance and $E_c = e^2/(4\pi\varepsilon_0\varepsilon d_{\mathrm{def}})$ the Coulomb interaction between neighboring dopants. Note

---

[*] grueninger@ph2.uni-koeln.de

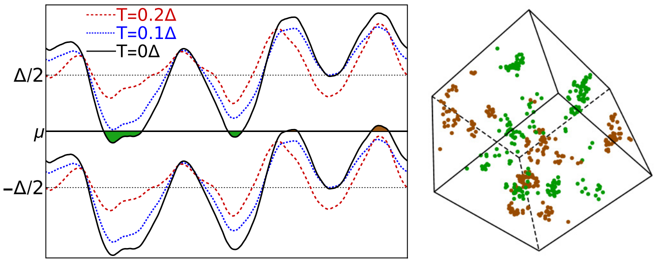

FIG. 1. Illustration of puddle formation. The left panel depicts the spatial variation of the energies $E_{\pm}(\mathbf{r}) = V(\mathbf{r}) \pm \Delta/2$ of conduction and valence bands (upper and lower lines) caused by the long-ranged Coulomb potential $V(\mathbf{r})$ arising from randomly placed donors and acceptors. At $T = 0$, the bands fluctuate so strongly that the chemical potential μ is crossed (shaded areas; data for $\Delta/E_c = 5$). This leads to the formation of metallic puddles, i.e., extended regions which are either n or p doped. An example is shown on the right ($T = 0$, $\Delta/E_c = 10$, green/brown: n/p doped). With increasing temperature, the fluctuations of the potential decrease (dashed lines in left panel) due to screening by thermally activated carriers thereby suppressing puddle formation.

that $R_g \gg d_{\text{def}}$ in the experimentally relevant regime $\Delta \gg E_c$ (typical values are $\Delta = 0.3$ eV and $E_c < 4$ meV for $N_{\text{def}} < 10^{20}\ \text{cm}^{-3}$ and $\varepsilon = 200$; see below). As a consequence, the valence and conduction bands are deformed so strongly that they touch and cross the chemical potential, giving rise to a redistribution of charges which modifies again the Coulomb potential. Electrically conducting puddles form as a result of this highly nonlinear self-organization process (see Fig. 1). In the case of electron puddles, for example, electrons confined within the puddle compensate the charge of some of the positive donors, creating charge-neutral donors (green areas in Fig. 1). If such a dramatic bending of the bands takes place, the aim of tuning the bulk chemical potential to a specific value relative to the band edge is doomed to failure.

Based on this puddle scenario, Shklovskii and coworkers [39] find activated behavior of the bulk resistivity, $\rho_b(T) \propto \exp(E_A/k_B T)$, with a *small* activation energy $E_A \approx 0.15\,\Delta$, consistent with experimental values [38]. Puddle formation is an intrinsic property of disordered Coulomb systems and a prime candidate to explain why it is so difficult to reach high bulk resistivities in compensated topological insulators. To examine the validity of the puddle scenario, a direct experimental detection of locally conducting puddles in the bulk of compensated topological insulators is highly desirable. Surface-sensitive techniques are not ideally suited, as puddles are strongly suppressed close to the metallic surface which provides an extra screening channel [40]. Nevertheless, the size of potential fluctuations observed in scanning tunneling microscopy [42] appears to be consistent with puddle formation [40].

Optical spectroscopy is a bulk-sensitive method ideally suited to detect large conducting regions. The optical properties of Bi_2Te_3, Bi_2Se_3, and of solid solutions thereof were investigated intensively already half a century ago [43–47] in view of their favorable thermoelectric properties [48,49]. Recently, optical data were reported for single crystals of Bi_2Te_2Se and $Bi_{2-x}Sb_xTe_{3-y}Se_y$ showing reduced carrier density [50–54]. However, the bulk carrier dynamics at very low densities were not addressed in detail. In particular, these data do not allow one to draw conclusions on the presence of puddles. Here, we give a detailed account of the optical properties of the approximately fully compensated topological insulator $BiSbTeSe_2$ in the infrared range. We reveal clear signatures of conducting puddles, making use of the recent achievement [38] of very low carrier densities in $BiSbTeSe_2$ and the sensitivity of transmittance measurements to weak absorption features. The corresponding spectral weight is strongly temperature dependent at low temperatures. Based on numerical simulations, we will argue that this temperature dependence is indeed characteristic of the mechanism of puddle formation by fluctuations of the Coulomb potential.

II. COMPENSATED $BiSbTeSe_2$

The binary tetradymites Bi_2Te_3 and Bi_2Se_3 can be categorized as degenerate semiconductors due to defect-induced charge carriers. Understanding the defect chemistry allowed for a dramatic reduction of the carrier density [4,55,56]. Near-stoichiometric Bi_2Se_3 exhibits n-type conductivity originating from Se vacancies acting as donors, whereas p-type conductivity predominates in Bi_2Te_3 due to antisite defects (i.e., Bi ions sitting on Te sites). The most successful route to reduced bulk conductivity aims at two goals in parallel: reduction of the defect density and compensation of the remaining defects, i.e., $K \equiv N_A/N_D = 1$. In $Bi_{2-x}Sb_xTe_{3-y}Se_y$, a reduced defect density is achieved by chalcogen order [37,38] (see Methods, Sec. VII A), while variation of both x and y allows for optimized compensation in combination with the possibility to independently tune the (average) energy of the Dirac point with respect to the Fermi energy E_F [57,58]. In particular, the Dirac point nearly coincides with E_F in $BiSbTeSe_2$, which means that this composition may serve as a benchmark for the bulk carrier dynamics at very low carrier concentrations with minimal contribution from the surface.

For a sample thickness $d \lesssim 10\,\mu$m, the bulk conductance of $Bi_{2-x}Sb_xTe_{3-y}Se_y$ is low enough at low temperatures to be out-weighted by the surface conductance [37,59,60]. This allows one, for example, to observe the half-integer quantum Hall effect on the topological surface state at temperatures up to 35 K [59]. Nonetheless, the bulk resistivity $\rho_b(T)$ in thick samples of $Bi_{2-x}Sb_xTe_{3-y}Se_y$ and also of Bi_2Te_2Se is puzzling, because it never exceeds 10–20 Ωcm [31,38,60–67] even after correcting for the shunting effect of the surface [60].

III. EXPERIMENTAL RESULTS

A. Optical spectroscopy

In single crystals of $BiSbTeSe_2$, the complex optical conductivity $\sigma_1(\omega) + i\sigma_2(\omega)$ was determined from infrared transmittance and reflectance data which were complemented at higher energies by ellipsometric measurements (see Methods, Sec. VII B). An overview of $\sigma_1(\omega)$ in the infrared range is plotted in Fig. 2 on a logarithmic scale. The spectra reveal the steep increase of $\sigma_1(\omega)$ caused by the onset of excitations across the gap Δ. At 5 K, we find $\Delta = 0.26$ eV ($2100\ \text{cm}^{-1}$). At 300 K, Δ is reduced by about 40%, it decreases with a slope of $\sim 3.6\ \text{cm}^{-1}/\text{K}$. Similar results for the temperature dependence

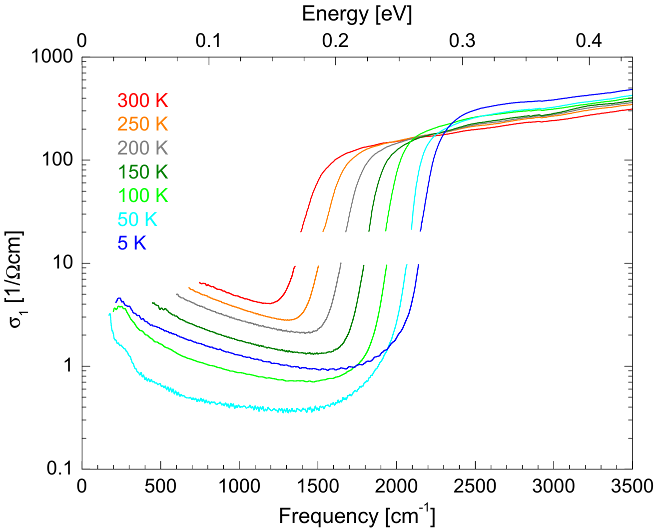

FIG. 2. Optical conductivity of BiSbTeSe$_2$ on a logarithmic scale. Weak absorption features below the gap with $\sigma_1(\omega) < 10\,(\Omega\text{cm})^{-1}$ were obtained from the transmittance $T(\omega)$ for a sample thickness of $d = 102\ \mu$m. For a given thickness, the frequency range in which the sample is transparent varies with temperature, see Fig. S1 in Supplemental Material [68]. Data with $\sigma_1(\omega) > 20\,(\Omega\text{cm})^{-1}$ in the opaque range were derived via a Kramers-Kronig analysis of the reflectivity. In combination, these data sets give an excellent account of $\sigma_1(\omega)$.

$\Delta(T)$ were reported for related topological insulators. For more details on $\Delta(T)$, see Supplemental Material [68].

The main focus of the present study is on the electronic contribution to the optical conductivity below the gap and its peculiar temperature dependence. In the temperature window from 40 to 60 K, $\sigma_1(\omega)$ reaches values as low as $0.3\,(\Omega\text{cm})^{-1}$. Most remarkably, the temperature dependence of $\sigma_1(\omega)$ is highly nonmonotonic. In the frequency range of about 300–1100 cm^{-1}, $\sigma_1(\omega)$ is more than three times *larger* at 5 K than at 50 K. The rise of $\sigma_1(\omega)$ upon heating above 50 K agrees with the dc conductivity $\sigma_1(\omega = 0)$ measured in transport, but the increase of $\sigma_1(\omega)$ upon cooling below 50 K strongly deviates from the transport results (see Fig. 3). At the same time, the spectral shape of $\sigma_1(\omega)$ below the gap is very similar at low and high temperatures, i.e., it can be described by a Drude peak with similar width (see below). In other words, the carrier density appears to display a nonmonotonic temperature dependence. We will show below that this feature and the discrepancy of dc and optical conductivities at low temperature are natural consequences of the carrier confinement within puddles and of the temperature dependence of puddle formation, providing the smoking gun for puddles.

Note that for all temperatures the measured values of $\sigma_1(\omega)$ below the gap are by far the lowest reported thus far for the entire family of Bi$_{2-x}$Sb$_x$Te$_{3-y}$Se$_y$. In Bi$_2$Te$_3$ and Bi$_2$Se$_3$, the Drude contribution of extrinsic carriers with typical densities $N \approx 10^{19}$ cm^{-3} extrapolates to dc values of $\sigma_1(0) \approx 1000\,(\Omega\text{cm})^{-1}$ [32,35,51,52,69–72]. In compounds with smaller N such as Bi$_2$Te$_2$Se, impurity absorption bands with peak values of 50–100 $(\Omega\text{cm})^{-1}$ were reported [50–52], one to two orders of magnitude larger than the conductivity observed by us. Such pronounced impurity bands are apparently absent in BiSbTeSe$_2$, in agreement with recent reflectivity data [54], which were, however, not sensitive enough to reveal the comparably weak absorption features with $\sigma_1(\omega) < 10\,(\Omega\text{cm})^{-1}$ observed by us in transmittance.

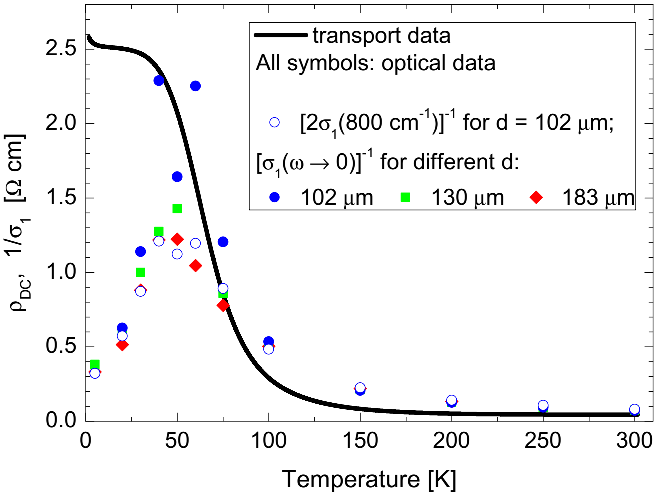

FIG. 3. Comparison of the dc resistivity of BiSbTeSe$_2$ with optical results. All data were obtained on pieces cut from the same crystal. Transport was measured on one piece, optical data on another piece which was thinned down subsequently; see Methods, Sec. VII B. Open symbols refer to $\sigma_1(\omega)$ at 800 cm^{-1} for the data plotted in Figs. 2 and 4. Drude fits to the data (cf. Fig. 4) roughly yield a peak width of 800 cm^{-1}. Therefore we plot $1/[2\sigma_1(800\text{cm}^{-1})]$, a rough estimate of the corresponding dc value. Full symbols denote the dc values obtained in these Drude fits on samples with different thicknesses. Above 50 K, transport and optical results agree within about a factor of 2, which strongly corroborates the assignment of the observed spectral weight to a Drude peak in this temperature range. At lower temperatures, carriers within puddles are indistinguishable from free carriers in the measured frequency range (see Sec. III C), but the strong discrepancy concerning the dc value is a very clear sign for puddle formation.

B. Absence of surface contributions

An important question is whether the spectral weight observed below the gap can be related to the surface states of the topological insulator. This can, however, be excluded by comparing data for different thicknesses d obtained successively on the same sample (see Methods, Sec. VII). Note that the transmittance depends exponentially on the thickness d. Neglecting any contribution of surface states in the analysis, results for $\sigma_1(\omega)$ for $d = 102$, 130, and 183 μm agree very well with each other within the experimental uncertainty of about 0.2 (Ωcm^{-1}) (see Fig. S3 in Supplemental Material [68]). This proves the bulk character of the excitations in the investigated frequency range. This conclusion has been confirmed by an analysis using an optical three-layer model in which the three layers correspond to the bulk and the two surfaces (see Supplemental Material [68]).

Theoretically, one may expect two contributions from the surface state: a Drude peak arising from surface conduction and *interband* excitations within the Dirac bands. In

BiSbTeSe$_2$, the Fermi level is close to the (average) position of the Dirac point [57], giving rise to a small density of surface states. Moreover, Dirac fermions show a large mobility. The respective narrow Drude peak is located below the frequency range addressed in our data, in agreement with terahertz data on thin films of Bi$_2$Se$_3$ and Bi$_{1.5}$Sb$_{0.5}$Te$_{1.8}$Se$_{1.2}$ [73,74]. *Interband* excitations within the Dirac bands contribute at higher frequencies. For $\hbar\omega \geqslant 2\,E_F$, a universal conductance $G_0 = \pi e^2/8h \approx 1.5 \times 10^{-5}/\Omega$ has been predicted [75,76]. For $d = 100\ \mu$m, this is equivalent to a bulk conductivity of 0.0015 $(\Omega\text{cm})^{-1}$, which is two orders of magnitude smaller than the lowest values observed in BiSbTeSe$_2$; see Fig. 2. We therefore conclude that all of our observations reflect bulk properties.

C. Electronic contribution to $\sigma_1(\omega)$

Figure 4 shows $\sigma_1(\omega)$ on a linear scale for frequencies below the gap. The broad electronic absorption feature is only observable in a frequency window where the sample is sufficiently transparent. This window is limited by strong phonon absorption at low frequencies and by excitations across the gap Δ at high frequencies. A particularly strong phonon mode can be identified in reflectivity data (see Fig. S6 in Supplemental Material [68]), it is located at about 70 cm^{-1} with a peak value of the order of 10^3 $(\Omega\text{cm})^{-1}$ [52,54]. In order to separate the electronic contribution, we first address $\sigma_1(\omega)$ at 40 K where the electronic contribution is the smallest and thus allows a clear view on the remaining features (see inset of Fig. 4). On top of the high-frequency tail of phonon absorption, we find a tiny absorption band extending up to about 350 cm^{-1} with a peak value of about 1 $(\Omega\text{cm})^{-1}$. Based on the frequency range and the tiny spectral weight, this can be attributed to a multiphonon contribution, i.e., two- and three-phonon excitations. The remaining contributions of electronic origin we fit with a tiny, temperature-independent constant term of about 0.2 $(\Omega\text{cm})^{-1}$ and a strongly temperature-dependent Drude peak. The tiny constant offset roughly corresponds to the experimental uncertainty.

Well above 50 K, the interpretation of the broad absorption feature as a Drude peak of thermally activated carriers is supported by the absolute value of $\sigma_1(\omega)$ (see Fig. 3), by the peak width, and by the temperature dependence of the spectral weight, as shown below. The main focus of our study is, however, on the reappearance of spectral weight at low temperatures, which can be attributed to locally n- or p-doped puddles. In the presence of puddles with a size smaller than the wavelength ($\lambda = 10\,\mu$m at 1000 cm^{-1}), the effective dielectric function ε_{eff} can be described by an effective medium approximation. Due to the large value of the dielectric function in BiSbTeSe$_2$, puddles can be taken into account by a simple additive oscillator term (see Supplemental Material [68]). Carriers localized in puddles do not contribute to the dc conductivity and thus have to be described by a Lorentzian oscillator. However, for frequencies above a cutoff ω_c given by the Thouless energy, the carriers within puddles are indistinguishable from free carriers, i.e., their contribution is expected to be of Drude form for $\omega \gg \omega_c$. The Thouless energy is determined by the time scale needed to diffuse through a puddle, $\omega_c = D/L^2$, where D denotes the diffusion constant and L the puddle size. Due to the large size of the puddles, the cutoff ω_c is expected to be more than three orders of magnitude smaller than the frequency range investigated by us. A rough estimate yields $\hbar\omega_c \leqslant 0.01$ meV (0.1 cm^{-1}); see Supplemental Material [68]. Accordingly, it is well justified to fit the data in the transparent range above 180 cm^{-1} with the Drude model also at low temperatures. The distinction between free carriers and localized carriers is then based on the comparison with dc resistivity data; see Fig. 3.

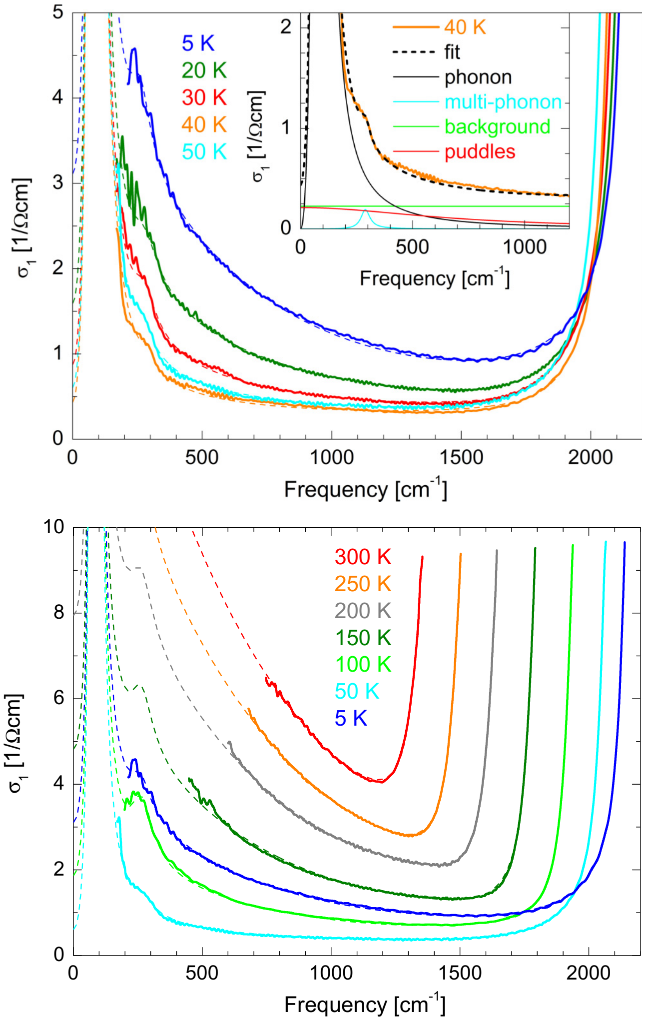

FIG. 4. Optical conductivity below the gap. At 40–50 K, $\sigma_1(\omega)$ is tiny below the gap. With increasing temperature, we identify a Drude peak of activated carriers with a strongly temperature-dependent spectral weight (see bottom panel and Fig. 5) and a large and approximately temperature-independent scattering rate, $1/\tau \approx 1.4 \times 10^{14}$ s^{-1}. Most remarkable is the reappearance of low-frequency spectral weight below about 50 K, which reveals the formation of puddles (see top panel). The inset shows a fit of the 40 K data where the broad low-frequency band of carriers localized within puddles (red) is smallest. This allows us to determine three further contributions: a phonon at 70 cm^{-1}, a multiphonon band at 275 cm^{-1}, and a tiny constant background of 0.23 $(\Omega\text{cm})^{-1}$. The phonon and the background are kept constant in the fits of the optical data measured at other temperatures (see Supplemental Material [68]). Dashed lines in both panels depict the fit curves.

TABLE I. Effective carrier densities $N_{\mathrm{eff}} = Nm_e/m^*$ and scattering rates for different compounds. Carrier densities from Refs. [32,50] were calculated from the unscreened plasma frequencies given there. In Ref. [70], the screened plasma frequency $\omega_p/\sqrt{\varepsilon_\infty}$ is given together with $\varepsilon_\infty = 29.5$ for Bi_2Se_3.

Compound	$N_{\mathrm{eff}}(10^{19}/\mathrm{cm}^3)$	$1/\tau(10^{12}/\mathrm{s})$	T (K)	Ref.
$BiSbTeSe_2$	0.02 / 0.6	140	50 / 300	This work
Bi_2Te_2Se	1.9	40	300	[50]
Bi_2Se_3	2.9; 18	4; 23	6; 300	[32]; [70]
Bi_2Te_3	33; 46	4.7; 5.6	10; 10	[69]; [71]

In the Drude model, $\sigma_1(\omega)$ depends on the scattering rate $1/\tau$ and the effective carrier density $N_{\mathrm{eff}} = N\, m_e/m^*$,

$$\sigma_1(\omega) = \frac{\sigma_1(0)}{1+\omega^2\tau^2} = \frac{N_{\mathrm{eff}}\, e^2\, \tau/m_e}{1+\omega^2\tau^2}, \tag{1}$$

where e and m_e denote charge and mass of a free electron, respectively, and m^* is the effective band mass. Well above 50 K, the fit results for $\sigma_1(0)$ are consistent with the dc resistivity (see Fig. 3). From the peak width we obtain $1/\tau \approx 1.4 \times 10^{14}\ \mathrm{s}^{-1}$ roughly independent of temperature as expected for a scattering mechanism arising from the random position of defects. Scattering rates of different compounds are compared in Table I. Compensated $BiSbTeSe_2$ shows the smallest carrier density and by far the largest value of $1/\tau$ which supports that defect scattering is dominant. We tentatively attribute the much lower scattering rates observed in compounds with higher carrier densities to an enhanced screening of defects by itinerant carriers. With a roughly temperature-independent scattering rate, the temperature-driven increase of the spectral weight above about 50 K corresponds to an increase of N_{eff} that can be described as activated behavior with an activation energy $E_A = 26$ meV $\approx 0.1\,\Delta$ (see inset of Fig. 5). This roughly agrees with $E_A = 31$ meV derived from the dc resistivity in the temperature range of 80–170 K. The small activation energy has been proposed to be a clear signature of strong Coulomb fluctuations [39,40].

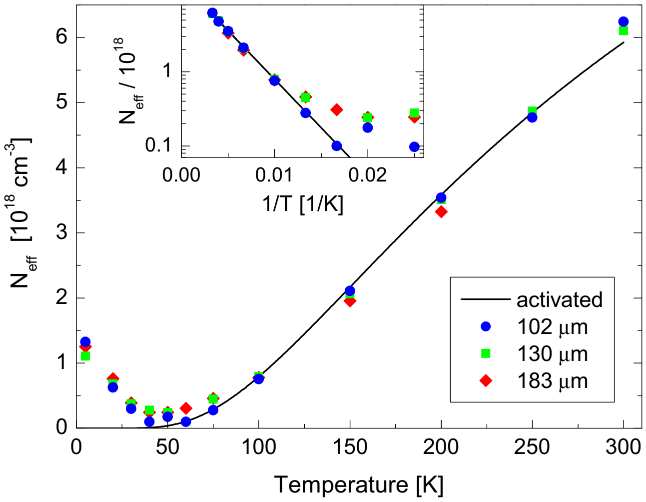

FIG. 5. Effective carrier density N_{eff}. Symbols depict fitting results for the low-frequency absorption band obtained for different sample thicknesses d. Below about 50 K, the carriers can be attributed to puddles. (Solid line) Activated behavior with an activation energy $E_A = 26$ meV. (Inset) Same data on a log scale vs $1/T$.

Combining our optical result for τ with the mobility $\mu = e\tau/m^* = 62\ \mathrm{cm}^2/\mathrm{Vs}$ obtained at 300 K in transport measurements on pieces cut from the same crystal, we may estimate the effective mass as $m^*/m_e \approx 0.2$. In $BiSbTeSe_2$, the cyclotron mass of the bulk bands is unknown since the measured quantum oscillations arise only from the surface states [38]. However, the cyclotron mass of the bulk conduction band has been measured in Bi_2Se_3, showing m^*/m_e between 0.14 and 0.24 depending on the orientation of the cyclotron orbit [34], in agreement with our result. Using $m^*/m_e = 0.2$, we deduce a carrier density as low as $N = N_{\mathrm{eff}}\, m^*/m_e \approx 4 \times 10^{16}\ \mathrm{cm}^{-3}$ between 40 and 60 K.

D. Puddles

Our main result is the dramatic reappearance of low-frequency spectral weight at temperatures below 50 K; see Fig. 5. The charge carriers responsible for this do, however, not contribute to the dc conductivity. The extrapolated low-frequency value of $\sigma_1(\omega)$ at 5 K is about an order of magnitude larger than the dc transport result for $\sigma_1(\omega = 0)$; see Fig. 3. This is consistent with a picture of well-separated metallic puddles contributing to $\sigma_1(\omega)$ but not directly to dc transport.

The effective carrier density amounts to $N_{\mathrm{eff,p}} \approx 1.2 \times 10^{18}\mathrm{cm}^{-3}$ at 5 K. Using the value of the effective mass determined at 300 K, this corresponds to an *average* carrier density $N_{\mathrm{p}} \approx 2.4 \times 10^{17}\mathrm{cm}^{-3}$, which is, however, expected to be distributed in a highly nonuniform way due to puddle formation. With increasing temperature, the carrier density shows a rapid drop by a factor of 4–6 at a temperature scale of the order of 30–40 K; see Fig. 5. Below we will show that this temperature scale has to be identified with the energy scale E_c, which agrees quantitatively with theoretical expectations. Also the average carrier density N_{p} can be explained by our numerical simulations.

Note that an unconventional–but much weaker–temperature dependence of the carrier density has been observed before in this family of topological insulators. In Bi_2Te_3, an unconventional decrease of N_{eff} by up to a factor of 2 has been observed between 5 and 300 K [69,71,72]. For compensated Bi_2Te_2Se with $N_{\mathrm{eff}} \approx 10^{19}\ \mathrm{cm}^{-3}$, a nonmonotonic behavior of N_{eff} with a minimum in the range of 50–150 K was reported [53]. However, N_{eff} in Bi_2Te_2Se changes by less than 10% between 5 and 50 K and by about 20% between 50 and 300 K, whereas we find a drastic change by more than a factor of 10 in $BiSbTeSe_2$; see Fig. 5. We emphasize that our results are based on samples with very low carrier density in combination with the enhanced sensitivity for weak absorption features offered by transmittance measurements.

IV. MODELING THE FORMATION AND DESTRUCTION OF PUDDLES

In order to describe the formation of puddles in a compensated semiconductor and in particular the temperature dependence observed in our optical data, we use a simple classical electrostatic model as discussed by Skinner, Chen, and Shklovskii [39]. The model assumes that donors and acceptors are located at random positions $\mathbf{r}_i$ in space. Their average densities are given by N_D and N_A, respectively, with $N_{\mathrm{def}} = (N_A + N_D)/2$. We address the experimentally relevant limit of almost perfect compensation where $K = N_A/N_D$ is close to 1. The binding energy of charges to defects is small due to the large static dielectric constant $\varepsilon \approx 200$ (see Supplemental Material [68]). A simple hydrogenlike model yields a binding energy of 1 Ry $\frac{m^*}{m}\frac{1}{\varepsilon^2} < 0.3$ meV $\approx 10^{-3}\Delta$, thus donors and acceptors are shallow with energy levels very close to $\pm\Delta/2$. This situation is described by the Hamiltonian,

$$H = \sum_i \frac{\Delta}{2} f_i n_i + \frac{1}{2}\sum_{i,j} V_{\mathbf{r}_i-\mathbf{r}_j} q_i q_j, \tag{2}$$

where $n_i = 0,1$ denotes the number of electrons on a donor ($f_i = 1$) or acceptor ($f_i = -1$) site. The charge of a donor (acceptor) amounts to $q_i = 1 (q_i = -1)$ if it has donated (accepted) an electron to (from) another defect, otherwise defects are charge neutral, $q_i = 0$. The Coulomb potential is supplemented by a short-distance cutoff a_B, $V_{\mathbf{r}_i-\mathbf{r}_j} = e^2/\{4\pi\varepsilon_0\varepsilon(|\mathbf{r}_i - \mathbf{r}_j|^2 + a_B^2)^{1/2}\}$, which effectively takes into account the finite extent of the wave functions of the shallow impurity states [39]. It was set to $a_B = 2/N_{\mathrm{def}}^{1/3}$ for all of our simulations. Expressing all distances in units of the average distance of dopants, $d_{\mathrm{def}} = 1/N_{\mathrm{def}}^{1/3}$, and all energies in units of the Coulomb interaction between neighboring dopants, $E_c = e^2/(4\pi\varepsilon_0\varepsilon d_{\mathrm{def}})$, all properties of the model depend on Δ/E_c, K, and T/E_c.

Besides the donor and acceptor states, no further conduction or valence electron states are taken into account in Eq. (2). For a gap of $\Delta/k_B \sim 3000$ K, the contribution of intrinsic carriers thermally activated across the gap can be neglected at low temperatures. Also the intrinsic carrier density within a puddle can be neglected. This is due to the small effective mass m^* in combination with the small value of the Fermi energy $E_F \sim E_c$ within the puddles (see below). Using $m^*/m_e = 0.2$ and $E_F = 50$ K for a single spherical band, one obtains an electron density of 10^{17} cm^{-3}, more than an order of magnitude smaller than the typical density of defects.

While the classical model of Eq. (2) is strongly simplified, it has been established as a powerful tool [36,39–41] which yields a semiquantitative understanding of puddle formation at $T = 0$. We reproduce the $T = 0$ results of Ref. [39], minimizing the energy by a pairwise exchange of charges. Most importantly, the model is sufficiently simple to allow for quantitative numerical simulations also at finite temperatures using a Monte Carlo approach (see Methods, Sec. VII C, and e.g., Ref. [77] for finite T simulations for other Coulomb systems). We obtain results with only small finite-size effects for values of Δ/E_c up to 25 (see Supplemental Material [68]).

Puddles are formed from occupied donor states or empty acceptor states (see Fig. 1). These correspond to *neutral* dopants, where, e.g., an electron compensates a positively charged donor ion. However, not all neutral dopants contribute to puddles which are *extended* regions of neutral dopants. These have to be distinguished from isolated sites which arise, e.g., due to thermal activation from an occupied acceptor to an empty donor. This distinction between isolated neutral dopants and puddles is achieved by counting the number of neutral dopants in the vicinity of a given neutral dopant (for details, we refer to the Supplemental Material [68]).

V. DISCUSSION

Our main experimental results are the presence of a sizable optical weight at low temperature and its rapid drop on a small temperature scale of the order of 30–40 K (see Fig. 5). We attribute this behavior to a pronounced temperature dependence of the average carrier density $N_p(T)$ of puddles. In the following we will show that our numerical simulations yield a semiquantitative description of the experimental results.

Figure 6 depicts numerical results for the fraction of dopants located in puddles, $p(T) = N_p(T)/N_{\mathrm{def}}$, for different values of Δ/E_c and $K \equiv N_A/N_D$. All of the data show a finite fraction of carriers inside of puddles at $T = 0$ as well as a strong reduction of $p(T)$ upon increasing T. Note that the *total* density of neutral dopants *increases* with increasing T due to thermal activation (see Supplemental Material [68]). Since the volume fraction of puddles is small, thermal activation predominantly occurs at isolated sites. These thermally activated charges screen the Coulomb potential, which leads to a pronounced reduction of the fluctuations of the Coulomb potential (see Fig. 1), and therefore to the destruction of puddles in a highly nonlinear process. Figure 6 demonstrates that this destruction of puddles occurs on a temperature scale which is set by the Coulomb interaction E_c between neighboring dopants. This temperature scale is remarkably robust against changes of

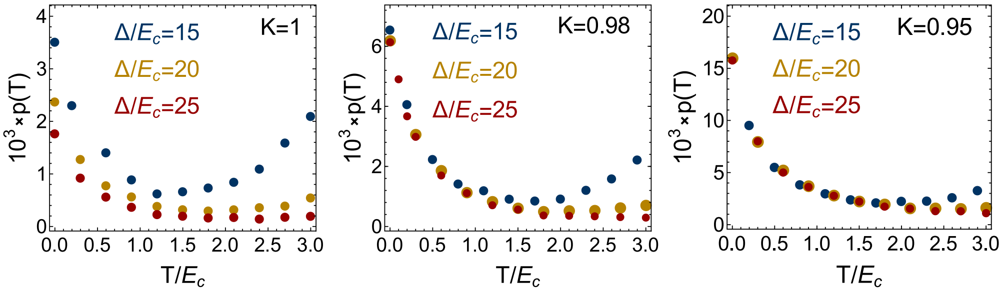

FIG. 6. Destruction of puddles with increasing temperature. The fraction $p(T)$ of dopants organized in puddles drops rapidly as a function of temperature at a temperature scale set by the Coulomb interaction E_c between neighboring dopants. This temperature scale is valid both for perfect compensation $K = 1$ (left panel) as well as for small deviations from $K = 1$ (middle, $K = 0.98$; right, $K = 0.95$). Numerical results are given for $\Delta/E_c = 15$, 20, and 25. Note that the increase of $p(T)$ for larger values of T/E_c and smaller values of Δ/E_c is due to thermal activation.

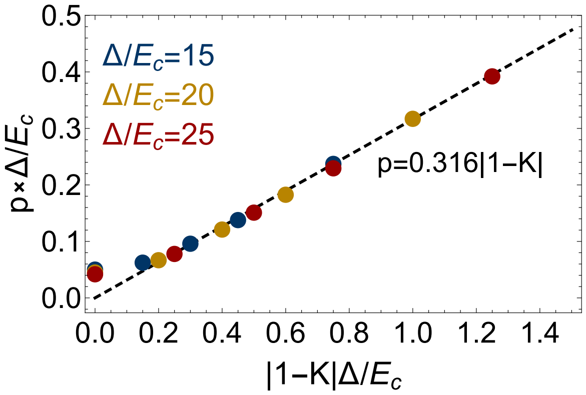

FIG. 7. Puddle formation and doping. At $T = 0$, the fraction p of dopants organized in puddles depends on Δ/E_c and on the degree of compensation $K = N_A/N_D$. However, plotting $p \cdot \Delta/E_c$ as a function of $|1-K|\,\Delta/E_c$ we obtain a scaling collapse for all values of Δ/E_c. In systems with small deviations $|1-K| \ll 1$ from perfect compensation, p rises linearly with increasing deviation, $p \approx 0.316\,|1-K|$ for $|1-K| \gtrsim 0.2\,E_c/\Delta$. In the experimentally relevant range of $\Delta/E_c = 75$–100, the linear regime is reached already for $K \leqslant 0.997$.

Δ/E_c and deviations from perfect compensation, at least in the investigated parameter regime ($|1-K| \ll 1$ and $\Delta \gg E_c$) which is relevant to our experimental data. Accordingly, we identify E_c with the experimentally observed temperature scale, $E_c/k_B = 30$–40 K (see Fig. 5). This translates to a ratio of $\Delta/E_c \approx 75$–100. Using

$$E_c = \frac{e^2}{4\pi\epsilon_0\epsilon} N_{\text{def}}^{1/3}, \tag{3}$$

with $\epsilon = 200$, we obtain the defect density $N_{\text{def}} = 4.6$–$11 \times 10^{19}\ \text{cm}^{-3}$. This is fully consistent with the carrier density observed in uncompensated samples; see Table I. This agreement indicates that the optical determination of E_c may turn out to be a useful tool to estimate the defect density N_{def}, a quantity which is difficult to assess in a compensated semiconductor.

In the next step, we address the absolute value of the spectral weight at low temperature. With the experimental results for $N_{\text{def}} = 4.6$–$11 \times 10^{19}\ \text{cm}^{-3}$ and the average carrier density $N_{\text{p}} \approx 2.4 \times 10^{17}\text{cm}^{-3}$ at 5 K (see Sec. III D), we find $p = N_p/N_{\text{def}} \approx 0.002$–$0.005$. Figure 6 suggests that this value is of the same order of magnitude as found numerically for small deviations from perfect compensation, i.e., $1 > K \gtrsim 0.98$. This is supported by Fig. 7 which shows a scaling collapse of all data at $T = 0$ when plotting $p \cdot \Delta/E_c$ vs $|1-K|\,\Delta/E_c$. For $K = 1$, we find $p \cdot \Delta/E_c \approx 0.06$, which is smaller than the experimental result 0.2–0.5. However, $p \cdot \Delta/E_c$ rapidly increases when small deviations from perfect compensation are taken into account. In the experimentally relevant range $p \cdot \Delta/E_c = 0.2$–0.5, we find a linear dependence $p = 0.316 \cdot |1-K|$ which is independent of Δ/E_c. This allows for a direct comparison of theory and experiment even in the experimentally relevant regime $\Delta/E_c = 75$–100. We find that a small deviation of $\lesssim 2\%$ from perfect compensation is sufficient to obtain a consistent description of the spectral weight observed at low temperature.

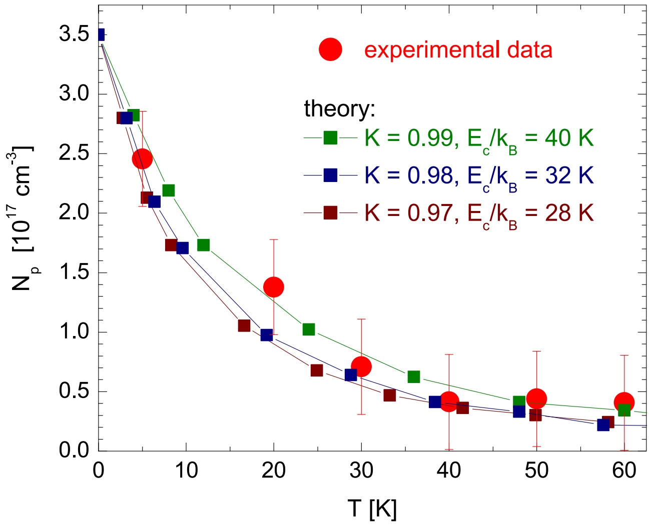

FIG. 8. Comparison of experimental and numerical results for the average carrier density $N_p(T)$ of puddles. At each temperature, we averaged over the results obtained for different sample thicknesses shown in Fig. 5, using $m^*/m_e = 0.2$. Error bars indicate the uncertainty arising from the fitting procedure (see Fig. 4). Excellent agreement between experiment and theory is obtained for $K = 0.98$–0.99.

The linear dependence $p \propto |1-K|$ sets in roughly when $|N_D - N_A|$, the uncompensated part of the doping, becomes larger than the density of neutral dopants organized in puddles at $K = 1$. This linear growth of p corresponds to the effect that adding, e.g., a small amount of extra donors to the perfectly compensated system does *not* give rise to a uniform doping but instead increases the number of neutral donors organized in puddles. This nonuniform doping originates again in the large-scale inhomogeneities of the Coulomb potential and is important also for the behavior at finite temperature.

Finally, we compare the numerical simulations with the experimental result for the temperature dependence $N_p(T)$. For $K = 0.98$–0.99 and $E_c/k_B = 32$–40 K, we find excellent agreement between experiment and theory (see Fig. 8). Our model thus is capable of describing the observed spectral weight as well as its evolution with temperature. This agreement clearly corroborates the existence of puddles in BiSbTeSe$_2$ and also confirms the scenario that they arise from strong fluctuations of the Coulomb potential. For any choice of $K < 0.997$, the value of $E_c \propto N_{\text{def}}^{1/3}$ is fixed by the low-temperature value of $N_p = p \cdot N_{\text{def}} = 0.316\,|1-K| \cdot N_{\text{def}}$ (see Fig. 7). For larger deviations $|1-K|$ from perfect compensation such as $K = 0.97$, we have to choose a value of E_c/k_B smaller than 30 K in order to describe the spectral weight at low temperatures. For such small values of E_c, however, the experimentally observed temperature dependence is not described very well anymore (see Fig. 8). We thus conclude that the degree of compensation K in our sample lies in the range 0.98–0.99, i.e., close to perfect compensation.

Taking both the extremely simplified nature of the theoretical description and the uncertainties in parameters like the effective mass into account, the quantitative determination of the parameters should perhaps not be taken too literally.

They are, however, highly plausible, suggesting that at low temperatures we achieve agreement between theory and experiment at least on a semiquantitative level.

VI. CONCLUSION

Our optical conductivity data of the almost perfectly compensated topological insulator $\mathrm{BiSbTeSe_2}$ reveal the existence of puddles at low temperatures as well as their destruction on a temperature scale of 30–40 K. The temperature dependence of the average carrier density of puddles, $N_p(T)$, is described very well by our numerical simulations based on a model of shallow donors and acceptors interacting by long-ranged Coulomb interactions. In particular, theory and experiment semiquantitatively agree on both the spectral weight and the temperature scale of puddle formation. We have shown that puddles are suppressed by thermally activated charges which screen the Coulomb potential. The temperature scale of puddle formation is set by the Coulomb interaction E_c between neighboring dopants. This mechanism works both for near-perfect and perfect compensation. Our approach builds on the Efros-Shklovskii theory, one of the central pillars for the description of disordered Coulomb systems. The result that thermal excitations lead to an efficient screening of long-range Coulomb fluctuations and thus to a breakdown of puddle formation is an important effect which is highly relevant for disordered Coulomb systems in general.

Puddle formation driven by long-ranged Coulomb interactions is not only of importance in compensated semiconductors but also for other materials with a vanishing density of electronic states including Dirac matter in two or three dimensions, like graphene [78] or Weyl semimetals. For the latter, it has been shown that long-range potential fluctuations as introduced by charged impurities have a large effect, giving rise to a finite density of states which smears out the differences between a Weyl semimetal and a real metal [79–81]. Furthermore, controlling puddles may turn out to be important for the experimental confirmation of the chiral anomaly, a well-known phenomenon in high-energy physics which is heavily sought after in condensed matter [82]. In Weyl semimetals, the observation of the chiral anomaly requires that the Fermi level is very close to the Dirac point. Band bending and puddle formation may therefore impede the observation of the chiral anomaly, even when the Fermi level is close to the average position of the Dirac point.

For the physics of topological insulators, puddle formation in compensated samples has both positive and negative effects. While the strong fluctuations of the Coulomb potential imply that it is more difficult to reach high bulk resistivities despite perfect compensation, they can also help to localize electrons or holes in puddles in situations where the compensation of donors and acceptors is not perfect. The surface states of topological insulators can provide extra screening channels, thus suppressing puddle formation close to the surface or in thin samples. It will therefore be interesting to study both experimentally and theoretically, how puddle formation depends on sample thickness and other parameters and how it interacts with the charge density of the topological surface states. Controlling puddle formation may turn out to be a key step for further reduction of bulk transport in topological insulators.

VII. METHODS

A. Samples

The compound $\mathrm{BiSbTeSe_2}$ belongs to the family of A_2B_3 tetradymites (A = Bi,Sb; B = Te,Se) showing rhombohedral structure (space group $R\bar{3}m$) [38,83] with three quintuple layers per unit cell stacked along the [111] direction. Single crystals of $\mathrm{BiSbTeSe_2}$ were grown starting from high-purity elements as described in Ref. [38]. The crystals were cut into platelets with typical dimensions of $3 \times 3\,\mathrm{mm}^2$ within the (111) plane. Due to the weak van der Waals bonding between quintuple layers, the samples can be cleaved easily along the (111) plane using adhesive tape. This yields shiny plane-parallel surfaces.

The defect chemistry of ternary compounds has been discussed in Ref. [56]. For quaternary $\mathrm{BiSbTeSe_2}$, one expects that donors are formed by Se and Te vacancies as well as by Te antisite defects on Bi(Sb) sites, while acceptors correspond to Bi and Sb vacancies as well as Bi(Sb) antisite defects on Te sites. The defect density can be reduced by chalcogen order $B^I - A - B^{II} - A - B^I$ within the quintuple layers [31,37,38,61]. In $\mathrm{Bi_2Te_2Se}$ with Te - Bi - Se - Bi - Te order [31,61], the B^{II} sites are exclusively occupied by Se ions. In the solid solutions $\mathrm{Bi_{2-x}Sb_xTe_{3-y}Se_y}$ with $y \geqslant 1$, the composition has been optimized with the aim to achieve full compensation [38,60]. Chalcogen order is preserved to some extent, as shown by x-ray diffraction [38]. Among these solid solutions, $\mathrm{BiSbTeSe_2}$ was reported to show the highest dc resistivity at 2 K [38]. It reaches 3 Ωcm but varies by about a factor of 3 for samples with the same nominal composition. This can partially be attributed to a thickness dependence [37,59,60] related to a finite conductance contribution of the surface but also reflects different defect concentrations [38].

B. Optical measurements

Infrared reflectance and transmittance measurements were performed with unpolarized light in the frequency range of 50–7500 cm^{-1} (6 meV–0.93 eV) using a Bruker IFS 66v/S Fourier-transform spectrometer equipped with a continuous-flow He cryostat. The transmittance $T(\omega)$ was recorded at normal incidence with the electric field parallel to the cleavage plane, while the reflectivity $R(\omega)$ was measured under near-normal incidence. Additionally, ellipsometric data were obtained using a rotating analyzer ellipsometer (Woollam VASE) equipped with a retarder between polarizer and sample. The ellipsometric data were collected at room temperature in the photon energy range of 0.75–5.5 eV (6050–44 360 cm^{-1}) for three different angles of incidence (60°, 70°, and 80°). Reflectance data and ellipsometric data were measured on a sample with a thickness of $d \approx 1.1$ mm. For the transmittance measurements, we started on a sample with a thickness of $d = (183 \pm 5)\,\mu\mathrm{m}$ (see Fig. S1 in Supplemental Material [68]). The value of d was determined mechanically using a micrometer screw. For this rather thick sample, the accuracy of 5 μm corresponds to an error of 2.7 %. Subsequently this sample was cleaved several times using adhesive tape, and the transmittance was measured successively on the same sample for a series of different thicknesses, $d = 183$, 130, and 102 μm. The latter two values were determined by comparing the Fabry-Perot interference fringes which arise in a transparent frequency range due to multiple reflections within the sample. Due to the shiny and plane-parallel surfaces obtained by cleaving, the interference fringes are particularly pronounced; see Fig. S1 in Supplemental Material [68]. For two samples a and b with different thicknesses d_a and d_b, the thickness ratio can be determined from the fringe periods, $\Delta\nu_a/\Delta\nu_b = d_b/d_a$, with an accuracy of better than 0.5 %. This is important for the comparison of results obtained for different thicknesses (see Fig. S3 in Supplemental Material [68]), and thus for the question whether there is a finite contribution of surface states.

In the transparent frequency range, the complex optical conductivity $\tilde{\sigma}(\omega) = \sigma_1(\omega) + i\sigma_2(\omega)$ can directly be determined from $T(\omega)$ and $R(\omega)$. The analysis is straightforward if one neglects interference effects and averages over the interference fringes by Fourier filtering [84]. The resulting complex $\tilde{\sigma}(\omega)$ has been tested by calculating, e.g., the transmittance including interference effects, which agrees nicely with the experimental data. In the opaque range, $\tilde{\sigma}(\omega)$ was obtained via a Kramers-Kronig analysis of the single-bounce reflectivity, i.e., the interference fringes need to be averaged by Fourier filtering. For the Kramers-Kronig analysis, we have used our results in the transparent range for the low-frequency extrapolation of $R(\omega)$, while the ellipsometric results have been employed for the high-frequency extrapolation.

C. Monte Carlo simulations

The model defined in Eq. (2) was simulated at finite T with a standard Monte Carlo algorithm (Metropolis). For $T = 0$ the algorithm is identical to the one used in Ref. [39]. It yields only a local and not a global minimum of the (free) energy but such pseudo-ground-states are known to describe the properties of real ground states with high accuracy [39].

Periodic boundary conditions for the Coulomb potential were imposed by using always the shortest distance on the 3-torus for its computation. We started the simulations from a configuration where all N_A acceptors and $(1 - K)\,N_D$ donors are occupied, such that the total system is charge neutral. We only considered configurations which keep charge neutrality by using a pairwise exchange of charge in each Metropolis step.

For $T \to 0$ we averaged over 300 disorder realizations. At finite temperatures, averages over 30 different realizations turned out to be sufficient. For the simulations at finite temperatures we used $2 \times 40^3 \approx 130\,000$ dopants for $\Delta/E_c = 15$, $2 \times 44^3 \approx 170\,000$ dopants for $\Delta/E_c = 20$, and $2 \times 48^3 \approx 220\,000$ dopants for $\Delta/E_c = 25$. For finite size checks we simulated up to $2 \times 64^3 \approx 520\,000$ dopants. Finite-size effects are largest for $K = 1, T = 0$, and $\Delta/E_c = 25$; see Supplemental Material [68] for details.

ACKNOWLEDGMENTS

Financial support through the German Excellence Initiative via the key profile area “quantum matter and materials” of the University of Cologne is gratefully acknowledged. The work was also supported by JSPS (Japan) (KAKENHI 25220708) and MEXT (Japan) (Innovative Area “Topological Materials Science” KAKENHI). The numerical simulations were performed on the CHEOPS cluster at RRZK Cologne.

[1] M. Z. Hasan and C. L. Kane, Colloquium: Topological insulators, Rev. Mod. Phys. **82**, 3045 (2010).

[2] X.-L. Qi and S.-C. Zhang, Topological insulators and superconductors, Rev. Mod. Phys. **83**, 1057 (2011).

[3] M. Z. Hasan and J. E. Moore, Three-dimensional topological insulators, Annu. Rev. Condens. Matter Phys. **2**, 55 (2011).

[4] Y. Ando, Topological insulator materials, J. Phys. Soc. Jpn. **82**, 102001 (2013).

[5] Y. Ando and L. Fu, Topological crystalline insulators and topological superconductors: From concepts to materials, Annu. Rev. Condens. Matter Phys. **6**, 361 (2015).

[6] S. Murakami, Phase transition between the quantum spin Hall and insulator phases in 3D: emergence of a topological gapless phase, New J. Phys. **9**, 356 (2007).

[7] X. Wan, A. M. Turner, A. Vishwanath, and S. Y. Savrasov, Topological semimetal and Fermi-arc surface states in the electronic structure of pyrochlore iridates, Phys. Rev. B **83**, 205101 (2011).

[8] O. Vafek and A. Vishwanath, Dirac fermions in solids: From high-T_c cuprates and graphene to topological insulators and Weyl semimetals, Annu. Rev. Condens. Matter Phys. **5**, 83 (2014).

[9] L. Fu, Topological Crystalline Insulators, Phys. Rev. Lett. **106**, 106802 (2011).

[10] T. H. Hsieh, H. Lin, J. Liu, W. Duan, A. Bansil, and L. Fu, Topological crystalline insulators in the SnTe material class, Nat. Commun. **3**, 982 (2012).

[11] Y. Tanaka, Z. Ren, T. Sato, K. Nakayama, S. Souma, T. Takahashi, K. Segawa, and Y. Ando, Experimental realization of a topological crystalline insulator in SnTe, Nat. Phys. **8**, 800 (2012).

[12] P. Dziawa, B. J. Kowalski, K. Dybko, R. Buczko, A. Szczerbakow, M. Szot, E. Łusakowska, T. Balasubramanian, B. M. Wojek, M. H. Berntsen, O. Tjernberg, and T. Story, Topological crystalline insulator states in $Pb_{1-x}Sn_xSe$, Nat. Mater. **11**, 1023 (2012).

[13] S.-Y. Xu, C. Liu, N. Alidoust, M. Neupane, D. Qian, I. Belopolski, J. D. Denlinger, Y. J. Wang, H. Lin, L. A. Wray, G. Landolt, B. Slomski, J. H. Dil, A. Marcinkova, E. Morosan, Q. Gibson, R. Sankar, F. C. Chou, R. J. Cava, A. Bansil, and M. Z. Hasan, Observation of a topological crystalline insulator phase and topological phase transition in $Pb_{1-x}Sn_xTe$, Nat. Commun. **3**, 1192 (2012).

[14] Z. Wang, Y. Sun, X.-Q. Chen, C. Franchini, G. Xu, H. Weng, X. Dai, and Z. Fang, Dirac semimetal and topological phase transitions in A_3Bi(A = Na,K,Rb), Phys. Rev. B **85**, 195320 (2012).

[15] Z. K. Liu, B. Zhou, Y. Zhang, Z. J. Wang, H. M. Weng, D. Prabhakaran, S.-K. Mo, Z. X. Shen, Z. Fang, X. Dai, Z. Hussain, and Y. L. Chen, Discovery of a three-dimensional topological Dirac semimetal, Na_3Bi, Science **343**, 864 (2014).

[16] S.-Y. Xu, C. Liu, S. K. Kushwaha, T.-R. Chang, J. W. Krizan, R. Sankar, C. M. Polley, J. Adell, T. Balasubramanian, K. Miyamoto, N. Alidoust, G. Bian, M. Neupane, I. Belopolski, H.-T. Jeng, C.-Y. Huang, W.-F. Tsai, H. Lin, F. C. Chou, T. Okuda, A. Bansil, R. J. Cava, and M. Z. Hasan, Observation of a bulk 3D Dirac multiplet, Lifshitz transition, and nestled spin states in Na_3Bi, arXiv:1312.7624.

[17] Z. Wang, H. Weng, Q. Wu, X. Dai, and Z. Fang, Three-dimensional Dirac semimetal and quantum transport in Cd_3As_2, Phys. Rev. B **88**, 125427 (2013).

[18] M. Neupane, S.-Y. Xu, R. Sankar, N. Alidoust, G. Bian, C. Liu, I. Belopolski, T.-R. Chang, H.-T. Jeng, H. Lin, A. Bansil, F. Chou, and M. Z. Hasan, Observation of a three-dimensional topological Dirac semimetal phase in high-mobility Cd_3As_2, Nat. Commun. **5**, 3786 (2014).

[19] S. Borisenko, Q. Gibson, D. Evtushinsky, V. Zabolotnyy, B. Büchner, and R. J. Cava, Experimental Realization of a Three-Dimensional Dirac Semimetal, Phys. Rev. Lett. **113**, 027603 (2014).

[20] M. Novak, S. Sasaki, K. Segawa, and Y. Ando, Large linear magnetoresistance in the Dirac semimetal TlBiSSe, Phys. Rev. B **91**, 041203(R) (2015).

[21] H. Weng, C. Fang, Z. Fang, B. A. Bernevig, and X. Dai, Weyl Semimetal Phase in Noncentrosymmetric Transition-Metal Monophosphides, Phys. Rev. X **5**, 011029 (2015).

[22] S.-M. Huang, S.-Y. Xu, I. Belopolski, C.-C. Lee, G. Chang, B. Wang, N. Alidoust, G. Bian, M. Neupane, C. Zhang, S. Jia, A. Bansil, H. Lin, and M. Z. Hasan, A Weyl Fermion semimetal with surface Fermi arcs in the transition metal monopnictide TaAs class, Nat. Commun. **6**, 7373 (2015).

[23] S.-Y. Xu, I. Belopolski, N. Alidoust, M. Neupane, G. Bian, C. Zhang, R. Sankar, G. Chang, Z. Yuan, C.-C. Lee, S.-M. Huang, H. Zheng, J. Ma, D. S. Sanchez, B. Wang, A. Bansil, F. Chou, P. P. Shibayev, H. Lin, S. Jia, and M. Z. Hasan, Discovery of a Weyl fermion semimetal and topological Fermi arcs, Science **349**, 613 (2015).

[24] B. Q. Lv, H. M. Weng, B. B. Fu, X. P. Wang, H. Miao, J. Ma, P. Richard, X. C. Huang, L. X. Zhao, G. F. Chen, Z. Fang, X. Dai, T. Qian, and H. Ding, Experimental Discovery of Weyl Semimetal TaAs, Phys. Rev. X **5**, 031013 (2015).

[25] L. X. Yang, Z. K. Liu, Y. Sun, H. Peng, H. F. Yang, T. Zhang, B. Zhou, Y. Zhang, Y. F. Guo, M. Rahn, D. Prabhakaran, Z. Hussain, S.-K. Mo, C. Felser, B. Yan, and Y. L. Chen, Weyl semimetal phase in the non-centrosymmetric compound TaAs, Nat. Phys. **11**, 728 (2015).

[26] B. Q. Lv, N. Xu, H. M. Weng, J. Z. Ma, P. Richard, X. C. Huang, L. X. Zhao, G. F. Chen, C. E. Matt, F. Bisti, V. N. Strocov, J. Mesot, Z. Fang, X. Dai, T. Qian, M. Shi, and H. Ding, Observation of Weyl nodes in TaAs, Nat. Phys. **11**, 724 (2015).

[27] S.-Y. Xu, N. Alidoust, I. Belopolski, Z. Yuan, G. Bian, T.-R. Chang, H. Zheng, V. N. Strocov, D. S. Sanchez, G. Chang, C. Zhang, D. Mou, Y. Wu, L. Huang, C.-C. Lee, S.-M. Huang, B. Wang, A. Bansil, H.-T. Jeng, T. Neupert, A. Kaminski, H. Lin, S. Jia, and M. Z. Hasan, Discovery of a Weyl fermion state with Fermi arcs in niobium arsenide, Nat. Phys. **11**, 748 (2015).

[28] A. C. Potter, I. Kimchi, and A. Vishwanath, Quantum oscillations from surface Fermi arcs in Weyl and Dirac semimetals, Nat. Commun. **5**, 5161 (2014).

[29] M. Stordeur, K. K. Ketavong, A. Priemuth, H. Sobotta, and V. Riede, Optical and electrical investigations of n-type Bi_2Se_3 single crystals, Phys. Status Solidi B **169**, 505 (1992).

[30] J. G. Analytis, R. D. McDonald, S. C. Riggs, Jiun-Haw Chu, G. S. Boebinger, and I. R. Fisher, Two-dimensional surface state in the quantum limit of a topological insulator, Nat. Phys. **6**, 960 (2010).

[31] Z. Ren, A. A. Taskin, S. Sasaki, K. Segawa, and Y. Ando, Large bulk resistivity and surface quantum oscillations in the topological insulator Bi_2Te_2Se, Phys. Rev. B **82**, 241306(R) (2010).

[32] A. D. LaForge, A. Frenzel, B. C. Pursley, Tao Lin, Xinfei Liu, Jing Shi, and D. N. Basov, Optical characterization of Bi_2Se_3 in a magnetic field: Infrared evidence for magnetoelectric coupling in a topological insulator material, Phys. Rev. B **81**, 125120 (2010).

[33] N. P. Butch, K. Kirshenbaum, P. Syers, A. B. Sushkov, G. S. Jenkins, H. D. Drew, and J. Paglione, Strong surface scattering in ultrahigh-mobility Bi_2Se_3 topological insulator crystals, Phys. Rev. B **81**, 241301(R) (2010).

[34] K. Eto, Z. Ren, A. A. Taskin, K. Segawa, and Y. Ando, Angular-dependent oscillations of the magnetoresistance in Bi_2Se_3 due to the three-dimensional bulk Fermi surface, Phys. Rev. B **81**, 195309 (2010).

[35] K. W. Post, B. C. Chapler, L. He, X. Kou, K. L. Wang, and D. N. Basov, Thickness-dependent bulk electronic properties in Bi_2Se_3 thin films revealed by infrared spectroscopy, Phys. Rev. B **88**, 075121 (2013).

[36] B. I. Shklovskii and A. L. Efros, Completely compensated crystalline semiconductor as a model of an amorphous semiconductor, Sov. Phys. JETP **35**, 610 (1972).

[37] A. A. Taskin, Z. Ren, S. Sasaki, K. Segawa, and Y. Ando, Observation of Dirac Holes and Electrons in a Topological Insulator, Phys. Rev. Lett. **107**, 016801 (2011).

[38] Z. Ren, A. A. Taskin, S. Sasaki, K. Segawa, and Y. Ando, Optimizing $Bi_{2-x}Sb_xTe_{3-y}Se_y$ solid solutions to approach the intrinsic topological insulator regime, Phys. Rev. B **84**, 165311 (2011).

[39] B. Skinner, T. Chen, and B. I. Shklovskii, Why is the Bulk Resistivity of Topological Insulators So Small?, Phys. Rev. Lett. **109**, 176801 (2012).

[40] B. Skinner, T. Chen, and B. I. Shklovskii, Effects of bulk charged impurities on the bulk and surface transport in three-dimensional topological insulators, J. Exp. Theor. Phys. **117**, 579 (2013).

[41] T. Chen and B. I. Shklovskii, Anomalously small resistivity and thermopower of strongly compensated semiconductors and topological insulators, Phys. Rev. B **87**, 165119 (2013).

[42] H. Beidenkopf, P. Roushan, J. Seo, L. Gorman, I. Drozdov, Y. S. Hor, R. J. Cava, and A. Yazdani, Spatial fluctuations of helical Dirac fermions on the surface of topological insulators, Nat. Phys. **7**, 939 (2011).

[43] J. Black, E. M. Conwell, L. Seigle, and C. W. Spencer, Electrical and optical properties of some $M_2^{V-B}N_3^{VI-B}$ semiconductors, J. Phys. Chem. Solids **2**, 240 (1957).

[44] I. G. Austin, The optical properties of bismuth telluride, Proc. Phys. Soc. London **72**, 545 (1958).

[45] D. L. Greenaway and G. Harbeke, Band structure of bismuth telluride, bismuth selenide and their respective alloys, J. Phys. Chem. Solids **26**, 1585 (1965).

[46] H. Gobrecht, S. Seeck, and T. Klose, Der Einflußder freien Ladungsträger auf die optischen Konstanten des Bi_2Se_3 im Wellenlängengebiet von 2 bis 23 μm, Z. Phys. **190**, 427 (1966).

[47] H. Köhler and C. R. Becker, Optically active lattice vibrations in Bi_2Se_3, Phys. Status Solidi B **61**, 533 (1974).

[48] B. Poudel, Q. Hao, Y. Ma, Y. Lan, A. Minnich, B. Yu, X. Yan, D. Wang, A. Muto, D. Vashaee, X. Chen, J. Liu, M. S. Dresselhaus, G. Chen, and Z. Ren, High-thermoelectric performance of nanostructured bismuth antimony telluride bulk alloys, Science **320**, 634 (2008).

[49] *Thermoelectric* Bi_2Te_3 *Nanomaterials*, edited by O. Eibl, K. Nielsch, N. Peranio, and F. Völklein (Wiley, New York, 2015).

[50] A. Akrap, M. Tran, A. Ubaldini, J. Teyssier, E. Giannini, D. van der Marel, P. Lerch, and C. C. Homes, Optical properties of Bi_2Te_2Se at ambient and high pressures, Phys. Rev. B **86**, 235207 (2012).

[51] P. Di Pietro, F. M. Vitucci, D. Nicoletti, L. Baldassarre, P. Calvani, R. Cava, Y. S. Hor, U. Schade, and S. Lupi, Optical conductivity of bismuth-based topological insulators, Phys. Rev. B **86**, 045439 (2012).

[52] A. A. Reijnders, Y. Tian, L. J. Sandilands, G. Pohl, I. D. Kivlichan, S. Y. Frank Zhao, S. Jia, M. E. Charles, R. J. Cava, N. Alidoust, S. Xu, M. Neupane, M. Z. Hasan, X. Wang, S. W. Cheong, and K. S. Burch, Optical evidence of surface state suppression in Bi-based topological insulators, Phys. Rev. B **89**, 075138 (2014).

[53] Yu. A. Aleshchenko, A. V. Muratov, V. V. Pavlova, Yu. G. Selivanov, and E. G. Chizhevskii, Infrared spectroscopy of Bi_2Te_2Se, JETP Lett. **99**, 187 (2014).

[54] K. W. Post, Y. S. Lee, B. C. Chapler, A. A. Schafgans, M. Novak, A. A. Taskin, K. Segawa, M. D. Goldflam, H. T. Stinson, Y. Ando, and D. N. Basov, Infrared probe of the bulk insulating response in $Bi_{2-x}Sb_xTe_{3-y}Se_y$ topological insulator alloys, Phys. Rev. B **91**, 165202 (2015).

[55] R. J. Cava, H. Ji, M. K. Fuccillo, Q. D. Gibson, and Y. S. Hor, Crystal structure and chemistry of topological insulators, J. Mater. Chem. C **1**, 3176 (2013).

[56] D. O. Scanlon, P. D. C. King, R. P. Singh, A. de la Torre, S. McKeown Walker, G. Balakrishnan, F. Baumberger, and C. R. A. Catlow, Controlling bulk conductivity in topological insulators: Key role of anti-site defects, Adv. Mater. **24**, 2154 (2012).

[57] T. Arakane, T. Sato, S. Souma, K. Kosaka, K. Nakayama, M. Komatsu, T. Takahashi, Z. Ren, K. Segawa, and Y. Ando, Tunable Dirac cone in the topological insulator $Bi_{2-x}Sb_xTe_{3-y}Se_y$, Nat. Commun. **3**, 636 (2012).

[58] M. Neupane, S.-Y. Xu, L. A. Wray, A. Petersen, R. Shankar, N. Alidoust, C. Liu, A. Fedorov, H. Ji, J. M. Allred, Y. S. Hor, T.-R. Chang, H.-T. Jeng, H. Lin, A. Bansil, R. J. Cava, and M. Z. Hasan, Topological surface states and Dirac point tuning in ternary topological insulators, Phys. Rev. B **85**, 235406 (2012).

[59] Y. Xu, I. Miotkowski, C. Liu, J. Tian, H. Nam, N. Alidoust, J. Hu, C.-K. Shih, M. Zahid Hasan, and Y. P. Chen, Observation of topological surface state quantum Hall effect in an intrinsic three-dimensional topological insulator, Nat. Phys. **10**, 956 (2014).

[60] Y. Pan, D. Wu, J. R. Angevaare, H. Luigjes, E. Frantzeskakis, N. de Jong, E. van Heumen, T. V. Bay, B. Zwartsenberg, Y. K. Huang, M. Snelder, A. Brinkman, M. S. Golden, and A. de Visser, Low carrier concentration crystals of the topological insulator $Bi_{2-x}Sb_xTe_{3-y}Se_y$: a magnetotransport study, New J. Phys. **16**, 123035 (2014).

[61] J. Xiong, A. C. Petersen, D. Qu, Y. S. Hor, R. J. Cava, and N. P. Ong, Quantum oscillations in a topological insulator Bi_2Te_2Se with large bulk resistivity (6 Ω cm), Physica E **44**, 917 (2012).

[62] J. Xiong, Y. Luo, Y. H. Khoo, S. Jia, R. J. Cava, and N. P. Ong, High-field Shubnikov–de Haas oscillations in the topological insulator Bi_2Te_2Se, Phys. Rev. B **86**, 045314 (2012).

[63] Z. Ren, A. A. Taskin, S. Sasaki, K. Segawa, and Y. Ando, Fermi level tuning and a large activation gap achieved in the topological insulator Bi_2Te_2Se by Sn doping, Phys. Rev. B **85**, 155301 (2012).

[64] S. Jia, H. Beidenkopf, I. Drozdov, M. K. Fuccillo, J. Seo, J. Xiong, N. P. Ong, A. Yazdani, and R. J. Cava, Defects and high bulk resistivities in the Bi-rich tetradymite topological insulator $Bi_{2+x}Te_{2-x}Se$, Phys. Rev. B **86**, 165119 (2012).

[65] C. Shekhar, C. E. ViolBarbosa, B. Yan, S. Ouardi, W. Schnelle, G. H. Fecher, and C. Felser, Evidence of surface transport and weak antilocalization in a single crystal of the Bi_2Te_2Se topological insulator, Phys. Rev. B **90**, 165140 (2014).

[66] A. Akrap, A. Ubaldini, E. Giannini, and L. Forro, $Bi_2Te_{3-x}Se_x$ series studied by resistivity and thermopower, Europhys. Lett. **107**, 57008 (2014).

[67] S. K. Kushwaha, Q. D. Gibson, J. Xiong, I. Pletikosic, A. P. Weber, A. V. Fedorov, N. P. Ong, T. Valla, and R. J. Cava, Comparison of Sn-doped and nonstoichiometric vertical-Bridgman-grown crystals of the topological insulator Bi_2Te_2Se, J. Appl. Phys. **115**, 143708 (2014).

[68] See Supplemental Material at http://link.aps.org/supplemental/10.1103/PhysRevB.93.245149 for transmittance spectra, the temperature dependence of the gap, the optical conductivity of samples with different thicknesses, the effective medium approximation for $BiSbTeSe_2$, a rough estimate of the Thouless energy, details on the fits of the low-temperature data, the reflectivity and the dielectric function in the far-infrared range, how to distinguish puddles from isolated sites, and a brief discussion of finite-size effects of the numerical data.

[69] G. A. Thomas, D. H. Rapkine, R. B. Van Dover, L. F. Mattheiss, W. A. Sunder, L. F. Schneemeyer, and J. V. Waszczak, Large electronic-density increase on cooling a layered metal: Doped Bi_2Te_3, Phys. Rev. B **46**, 1553 (1992).

[70] A. Segura, V. Panchal, J. F. Sánchez-Royo, V. Marín-Borrás, V. Muñoz-Sanjosé, P. Rodríguez-Hernández, A. Muñoz, E. Pérez-González, F. J. Manjón, and J. González, Trapping of three-dimensional electrons and transition to two-dimensional transport in the three-dimensional topological insulator Bi_2Se_3 under high pressure, Phys. Rev. B **85**, 195139 (2012).

[71] S. V. Dordevic, M. S. Wolf, N. Stojilovic, Hechang Lei, and C. Petrovic, Signatures of charge inhomogeneities in the infrared spectra of topological insulators Bi_2Se_3, Bi_2Te_3 and Sb_2Te_3, J. Phys.: Condens. Matter **25**, 075501 (2013).

[72] B. C. Chapler, K. W. Post, A. R. Richardella, J. S. Lee, J. Tao, N. Samarth, and D. N. Basov, Infrared electrodynamics and ferromagnetism in the topological semiconductors Bi_2Te_3 and Mn-doped Bi_2Te_3, Phys. Rev. B **89**, 235308 (2014).

[73] R. Valdés Aguilar, A. V. Stier, W. Liu, L. S. Bilbro, D. K. George, N. Bansal, L. Wu, J. Cerne, A. G. Markelz, S. Oh, and N. P. Armitage, Terahertz Response and Colossal Kerr Rotation

from the Surface States of the Topological Insulator Bi_2Se_3, Phys. Rev. Lett. **108**, 087403 (2012).

[74] C. S. Tang, B. Xia, X. Zou, S. Chen, H.-W. Ou, L. Wang, A. Rusydi, J.-X. Zhu, and E. E. M. Chia, Terahertz conductivity of topological surface states in $Bi_{1.5}Sb_{0.5}Te_{1.8}Se_{1.2}$, Sci. Rep. **3**, 3513 (2013).

[75] D. Schmeltzer and K. Ziegler, Optical conductivity for the surface of a topological insulator, arXiv:1302.4145.

[76] Zhou Li and J. P. Carbotte, Hexagonal warping on optical conductivity of surface states in topological insulator Bi_2Te_3, Phys. Rev. B **87**, 155416 (2013).

[77] M. Sarvestani, M. Schreiber, and T. Vojta, Coulomb gap at finite temperatures, Phys. Rev. B **52**, R3820(R) (1995).

[78] J. Martin, N. Akerman, G. Ulbricht, T. Lohmann, J. H. Smet, K. von Klitzing, and A. Yacoby, Observation of electron-hole puddles in graphene using a scanning single-electron transistor, Nat. Phys. **4**, 144 (2008).

[79] B. Skinner, Coulomb disorder in three-dimensional Dirac systems, Phys. Rev. B **90**, 060202(R) (2014).

[80] Ya. I. Rodionov and S. V. Syzranov, Conductivity of a Weyl semimetal with donor and acceptor impurities, Phys. Rev. B **91**, 195107 (2015).

[81] D. A. Pesin, E. G. Mishchenko, and A. Levchenko, Density of states and magnetotransport in Weyl semimetals with long-range disorder, Phys. Rev. B **92**, 174202 (2015).

[82] P. Hosur and X. Qi, Recent developments in transport phenomena in Weyl semimetals, C. R. Phys. **14**, 857 (2013).

[83] S. Nakajima, The crystal structure of $Bi_2Te_{3-x}Se_x$, J. Phys. Chem. Solids **24**, 479 (1963).

[84] M. Grüninger, M. Windt, T. Nunner, C. Knetter, K. P. Schmidt, G. S. Uhrig, T. Kopp, A. Freimuth, U. Ammerahl, B. Büchner, and A. Revcolevschi, Magnetic excitations in two-leg spin 1/2 ladders: experiment and theory, J. Phys. Chem. Solids **63**, 2167 (2002).